GEOPHYSICS, VOL. 65, NO. 5 (SEPTEMBER-OCTOBER 2000); P. 1613–1621, 11 FIGS., 2 TABLES.

Physical and numerical modeling of tuning and diffraction in azimuthally anisotropic media

Richard L. Gibson*, Jr., Stephen Theophanis‡, and M. Nafi Toksöz**

ABSTRACT

Fractured reservoirs are an important target for exploration and production geophysics, and the azimuthal anisotropy often associated with these reservoirs can strongly influence seismic wave propagation. We created a physical model of a fractured reservoir to simulate some of these propagation effects. The reservoir is represented by a phenolite disk that is thin with respect to the elastic wavelengths in the experiment, creating model dimensions that are representative of realistic reservoirs. Phenolite is strongly anisotropic with orthorhombic symmetry, which suggests that azimuthal amplitude versus offset (AVO) effects should be obvious in data. We acquired both *SH*- and *P*-wave data in common-offset gathers with a near offset and a far offset and found that although the *SH*-wave data show clear azimuthal variations in AVO, the *P*-wave signals show no apparent changes with azimuth.

We then applied numerical modeling to analyze the data. Because ray methods cannot model diffractions from the disk edge, we first used a ray–Born technique to simulate variations in waveforms associated with such scattering. The synthetic seismograms reproduced variations in the *SH*-wave waveforms accurately, though the amplitude contrast between acquisition azimuths was overestimated. Assuming a laterally homogeneous model, we then applied ray methods to simulate tuning effects in *SH*- and *P*-wave data and confirmed that in spite of the large contrasts in elastic properties, the tuning of the *P*-wave reflections from the thin disk changed so there was negligible contrast in AVO with azimuth. Models of field scale reservoirs showed that the same effects could be expected for field applications.

INTRODUCTION

Natural fracturing can be the dominant controlling factor for hydrocarbon production in many reservoirs. While it is possible to detect this fracturing in situ by logging or core sampling, these procedures are subject to significant uncertainty because of the damage caused by drilling. Equally important, such invasive procedures provide information only at the borehole itself, though the distribution and orientation of fractures throughout the reservoir are important in determining reservoir performance.

Seismic methods have the potential to offer more comprehensive information about the location and characterization of fractured zones. There have been many analyses of the effects of anisotropic layers on the propagation of elastic waves in both synthetic seismograms and in field data (Crampin, 1978, 1981; Leary and Henyey, 1985; Winterstein, 1986; Thomsen, 1988; Schoenberg and Helbig, 1997). Some recent work has focused on the kinematic aspects of propagation in azimuthally anisotropic media (Tsvankin, 1997; Al-Dajani and Tsvankin, 1998; Grechka et al., 1999). Much research has also focused on the phenomenon of shear-wave splitting (birefringence), which in many cases causes distinctive anomalies in the polarization of shear-wave arrivals (Martin and Davis, 1987; Lewis et al., 1991; Lefeuvre et al., 1993; MacBeth et al., 1994, Meadows and Winterstein, 1994). Shear-wave splitting is, in fact, the most distinctive property of anisotropic seismic wave propagation. This approach is most useful when the anisotropic, fractured region is thick enough and velocity contrast between the two split shear waves is large enough that a significant traveltime difference between the two arrivals results. In this case, polarization anomalies can be resolved easily.

However, many gas-containing reservoirs are not fractured uniformly and the fractured regions are small and thin, perhaps on the order of 10 m thick. At the same time, *P*-wave

Manuscript received by the Editor December 28, 1998; revised manuscript received January 12, 2000.
*Texas A&M University, Dept. of Geology and Geophysics, MS 3115, College Station, Texas 77843-3115. E-mail: gibson@nyssa.tamu.edu.
‡Formerly Science Research Laboratory, 15 Ward St., Somerville, Massachusetts 02143; presently Naval Research Laboratory, Code 7432, Stennis Space Center, Mississippi 39529. E-mail: theophanis@nrlssc.navy.mil.
**Earth Resources Laboratory, Massachusetts Institute of Technology, 42 Carleton St., Cambridge, Massachusetts 02142. E-mail: nafi@erl.mit.edu.

data acquisition is more economic, which suggests an examination of the utility of *P*-wave reflection data in the characterization of fractured reservoirs. Recent work has emphasized both theoretical descriptions of the azimuthal variations in reflection amplitude that should be present in fractured reservoirs (Mallick and Fraser, 1991; Rüger and Tsvankin, 1997; Rüger, 1998) and examinations of field data to confirm that such variations can be detected (Lynn et al., 1995; Johnson, 1995; Pérez et al., 1999). Such azimuthal variations would provide a comparatively economical and efficient tool for the characterization of fractured reservoirs. This provides the primary motivation for our work, where we compare azimuthal variations in the amplitude versus offset (AVO) response in *P*- and *S*-wave data acquired from a physical model of a fractured reservoir that is both three dimensional and thin compared to a wavelength.

In the following sections, we first describe the model and data acquisition procedures. We then examine the ultrasonic data, which show significant variations in reflection amplitude with azimuth for horizontally polarized shear waves (*SH*-waves) but negligible changes in *P*-wave amplitude. In addition, both *SH*- and *P*-wave data show changes in pulse shape as well as amplitude as the source–receiver pair moves across the disk. Two numerical modeling approaches are used to help interpret these phenomena. A ray–Born technique is used to simulate the changes in *SH*-wave signals, including the influence of diffractions from the disk edge. Ray methods are applied to model the tuning of reflections from the top and bottom of the disk for both *SH*- and *P*-wave data. We show that the azimuthal variations in tuning cancel out any changes in *P*-wave amplitude that occur because of changes in reflection coefficients, and we conclude with some discussion of possible applications of these results to field data.

PHYSICAL MODEL AND DATA

Our physical model contains a strongly anisotropic disk representing a reservoir surrounded by an isotropic medium (Figure 1). Two primary criteria were applied in the design of this model. First, the model reservoir was constrained to be relatively thin compared to the dominant wavelength of propagating body waves. Second, we chose to investigate lateral heterogeneity. For these reasons, the reservoir layer was modeled as a thin disk, which is simple to work with yet displays the desired lateral and vertical variations in material properties.

Subscale ultrasound experiment

The isotropic part of the model is constructed of five blocks of lucite that are 30.5 cm (12 inches) in width and depth, with a thickness of 7.6 cm (3 inches). These individual blocks were bonded with epoxy for a total height of 38.1 cm (15 inches) (Figure 1). Lucite was chosen for the background material because of its homogeneous, isotropic velocity and for its low cost and machinability. The epoxy bonding of all the joints was performed under a uniform pressure of 15 psi. The reflection coefficient for the epoxy joints between lucite layers was tested with both *P*- and *S*-waves of the appropriate frequencies and was found to be insignificant. Embedded 15.24 cm (6 inches) from the surface of this background is the disk representing the fractured zone. This disk measures 10.16 cm (4 inches) in diameter and is made of phenolite, a composite material with orthorhombic symmetry (Schoenberg and Helbig, 1997). This model is analogous to a fractured reservoir in that it includes azimuthal anisotropy, which is consistent with equivalent medium models of materials with vertically aligned fractures (Crampin, 1981). The elastic constants for phenolite are shown in Table 1, and phase velocities are plotted in Figure 2. The phenolite layer is bonded to the background material, aligned with its slow axis parallel to the model's *x*-axis, using the same epoxy bonding technique to ensure that reflections from the layer are not influenced by the joint. The physical properties of lucite are *P*-wave velocity, 2750 m/s; *S*-wave velocity, 1376 m/s; and density, 1190 kg/m^3.

Table 1. Physical properties of phenolite. Phase velocities are shown in Figure 2.

Property	Phenolite XX-324 value
C_{11}	10.1 GPa
C_{12}	7.9
C_{13}	7.3
C_{22}	17.5
C_{23}	11.5
C_{33}	20.8
C_{44}	5.1
C_{55}	2.63
C_{66}	2.63
Density	1340 kg/m^3

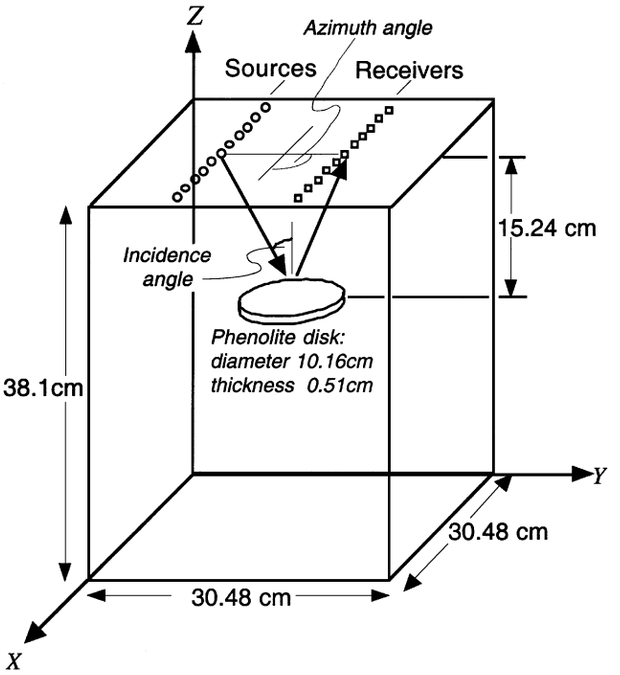

FIG. 1. Scale model used to acquire ultrasonic *P*- and *S*-wave data. The phenolite disk serves as an analog to a fractured reservoir in that it displays azimuthal anisotropy. Its thickness was chosen to be approximately five times smaller than a wavelength. Data were acquired for constant-offset source–receiver configurations such as the one shown schematically in this figure. Angle of incidence for the experiments was set to 10° and 45°, and the azimuthal angle was 0° and 90°.

Instrumentation

Ultrasonic transducers were chosen to produce an elastic wavelength approximately five times the layer thickness. This wavelength corresponds to frequencies of approximately 85 kHz for *S*-waves and 200 kHz for *P*-waves (Figure 3). Conveniently, this frequency range is close to that of conventional nondestructive testing (NDT) instrumentation, and suitable instruments were easy to obtain. Both the *P*- and the *S*-wave contact transducers, from Panametrics, measured 2.54 cm (1 inch) in diameter. The *P*-wave transducer produces and records primarily vertical vibrations, while the *S*-wave transducer moves horizontally. The center frequency and bandwidth of these transducers are adjustable, within limitations, by varying the width of the excitation pulse. The excitation pulse was provided by a Hewlett Packard 214B high-voltage pulse generator, which has independent control of voltage, pulse width, and repetition rate. Data were collected directly from the receiving transducer with a Lecroy 9304A oscilloscope, which has real-time signal averaging capability for noise reduction and a disk drive for data storage.

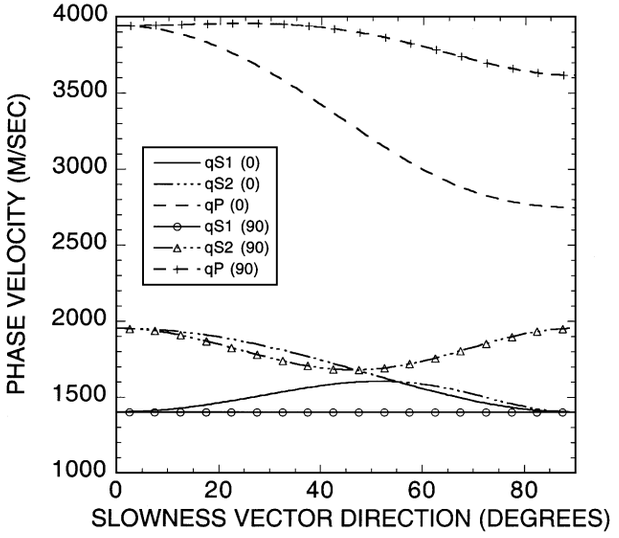

FIG. 2. Variation of phase velocity in phenolite for the quasi-compressional wave (*qP*) and the two quasi-shear waves (*qS*1, the slower wave, and *qS*2, the faster quasi-shear wave). Elastic constants are shown in Table 1.

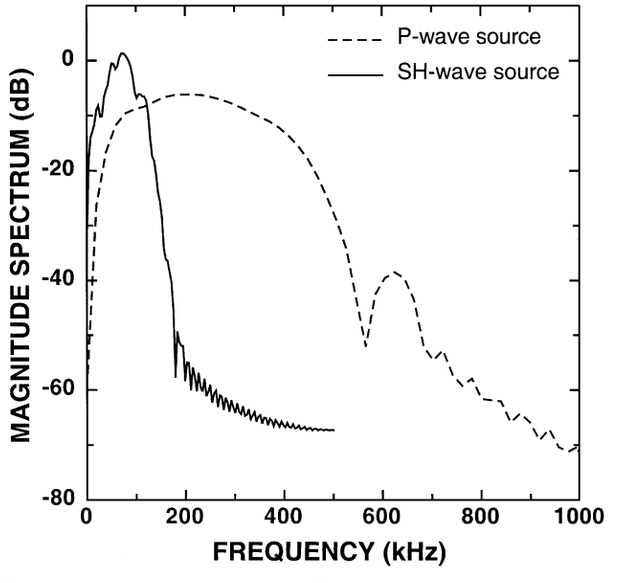

FIG. 3. Spectra of the *SH*- and *P*-wave source signals used in the experiments.

Model reflection survey data were collected using common-offset acquisition geometries. First, the source–receiver spacing was set to 2.7 cm (1.05 inches), corresponding to an angle of incidence of 10° for rays striking the phenolite disk. With this constant separation, the source and receiver transducers were moved along the centerline of the model's surface through a series of shotpoints crossing the disk, as indicated in Figure 1. We refer to the configuration with the source and receiver moved in the direction parallel to the *x*-axis as the 90° azimuth experiment because the seismic propagation direction is along the *y*-axis. The experiment was then repeated, moving the source–receiver pair parallel to the *y*-axis (the 0° azimuth experiment). When the transducers are over the middle of the model, the specular reflection point is therefore in the middle of the disk for both the 0° and the 90° configurations. This experiment was also performed with a source–receiver offset of 30.48 cm (12 inches), corresponding to a 45° angle of incidence. The end result for *P*-waves is a set of four constant-offset data sets, and analogous data were collected with the *S*-wave source and receiver transducers arranged to acquire *SH*-waves. Each data trace that we display is the average of 100 recordings, so the S/N ratio is very good and the data are highly repeatable.

NUMERICAL MODELING

Modeling of seismic wave propagation in complex, 3-D hydrocarbon reservoirs and in our physical model is difficult because of the small feature size in a large model relative to a seismic wavelength. Direct solution of the wave equation with finite differences is generally impractical because of the large computational resources required. This brute force approach requires both a fast supercomputer and large memory resources to hold the numerous parameters associated with anisotropic, elastic wave propagation. Ray tracing, on the other hand, can be applied to simulate 3-D wave propagation quite rapidly, but it is restricted to models where layer properties are smoothly varying because of the assumptions implicit in the asymptotic solution to the wave equation (Červený, 1985; Ben-Menahem and Beydoun, 1985). Interfaces can be included as long as ray amplitudes and directions are appropriately transformed across boundaries. Conventional ray tracing can therefore model reflections from the top and bottom of our physical model but cannot be applied to simulate diffractions from the edges of the disk representing the reservoir.

An alternative solution is the ray–Born algorithm (Beydoun and Mendes, 1989; Gibson et al., 1993), a hybridization of ray tracing with the analytic Born approximation. While the ray-tracing models propagation in a predefined, smoothly varying background medium, the Born approximation is a perturbation solution that yields approximate results for weak scattering of waves by localized variations in earth properties (Wu and Aki, 1985; Burridge and Beylkin, 1990; Gibson and Ben-Menahem, 1991). The material properties are described in the following

form, where $c_{ijkl}(\mathbf{x})$ are the elastic constants and $\rho(\mathbf{x})$ is density:

$$c_{ijkl}(\mathbf{x}) = c^0_{ijkl}(\mathbf{x}) + \delta c_{ijkl}(\mathbf{x}),$$
$$\rho(\mathbf{x}) = \rho^0(\mathbf{x}) + \delta\rho(\mathbf{x}). \quad (1)$$

The superscript 0 indicates the background model, and the small perturbations are $\delta c_{ijkl}(\mathbf{x})$ and $\delta\rho(\mathbf{x})$.

Assuming that the perturbations in velocity and density are small, the Born approximation then gives the perturbations $\delta u_i(\mathbf{x}, t)$ to the background displacement fields $u^0(\mathbf{x}, t)$ in the following form (Burridge and Beylkin, 1990):

$$u_i(\mathbf{x}, t) = -\int_{V(\mathbf{x}')} G^0_{ij}(\mathbf{x}, t \mid \mathbf{x}', t') * [M_{jk}(\mathbf{x}', t')s_k(\mathbf{x}')] + G^0_{ij}(\mathbf{x}, t \mid \mathbf{x}', t') * [f_j(\mathbf{x}', t')]\, dV(\mathbf{x}'), \quad (2)$$

$$M_{jk}(\mathbf{x}', t') = \delta c_{jklm}(\mathbf{x}')E^0_{lm}(\mathbf{x}', t'), \quad (3)$$

$$f_j(\mathbf{x}', t') = \partial^2_{tt}u^0_j(\mathbf{x}', t')\delta\rho(\mathbf{x}'), \quad (4)$$

where $*$ denotes temporal convolution and Einstein summation notation is assumed. Here, $G^0_{ij}(\mathbf{x}, t \mid \mathbf{x}', t')$ is the Green's tensor corresponding to propagation in the background medium from a source at $\mathbf{x}', t'$ to an observer at $\mathbf{x}, t$. Strain associated with this wavefield is E^0_{jk}. Equation (2) reveals several important aspects of the implementation and accuracy of the Born solution. First, the only Green's tensor appearing in this equation is that for the background medium, and the secondary source terms involve only displacements associated with the background field. This greatly simplifies and accelerates the modeling. The other primary issue for accuracy is the validity of the Born approximation itself. In general, the perturbations to the elastic constants and density should be relatively weak so that perturbations to displacements are also relatively small (Hudson and Heritage, 1981). This also implies that the thickness of the perturbed region relative to the propagation direction should be small, especially when perturbations are stronger (Beydoun and Tarantola, 1988). Because all propagation occurs in the background, phase corrections (i.e., traveltimes) associated with the perturbations are not modeled by the Born approximation, and these errors become large when the material perturbations extend over large regions.

Because the background for the phenolite disk model, the lucite, is homogeneous, the ray-theoretical Green's tensors are easily evaluated with analytic solutions for our application. The perturbations used in equation (2) are the difference between the elastic constants and density of phenolite and the corresponding values for lucite. Additional information regarding the implementation of the algorithm can be found in Gibson et al. (1993) and Beydoun and Mendes (1989).

In the following sections, we utilize the ray–Born approach to model 3-D propagation in the physical model, which successfully accounts for the changes in reflected wavefields as the source–receiver transducer pair moves across the phenolite disk. Because of the phase correction errors associated with the Born approximation, this method will not properly model the tuning of reflections from the top and bottom of the phenolite disk layer. We found that this tuning phenomenon plays a particularly important role in controlling the dependence of *P*-wave AVO on azimuth. Therefore, even though classical ray tracing cannot model the lateral amplitude variations associated with diffraction phenomena, we will apply it to simulate the azimuthal variations in tuning in the model.

SH-wave data and ray–Born results

SH-wave ultrasonic data for the common-offset gather collected with a 10° angle of incidence are shown in Figure 4 along with the ray–Born synthetic seismograms. The signal radiated by the *S*-wave transducer, with its dominant frequency of about 85 kHz, was included in the ray–Born computations so that the synthetic seismograms and the observed data should be directly comparable. The data and synthetics match well, and some of the subtle details of the data are closely reproduced in the modeling. For example, close comparison of the center trace (distance = 0 cm) with the adjacent traces shows that the

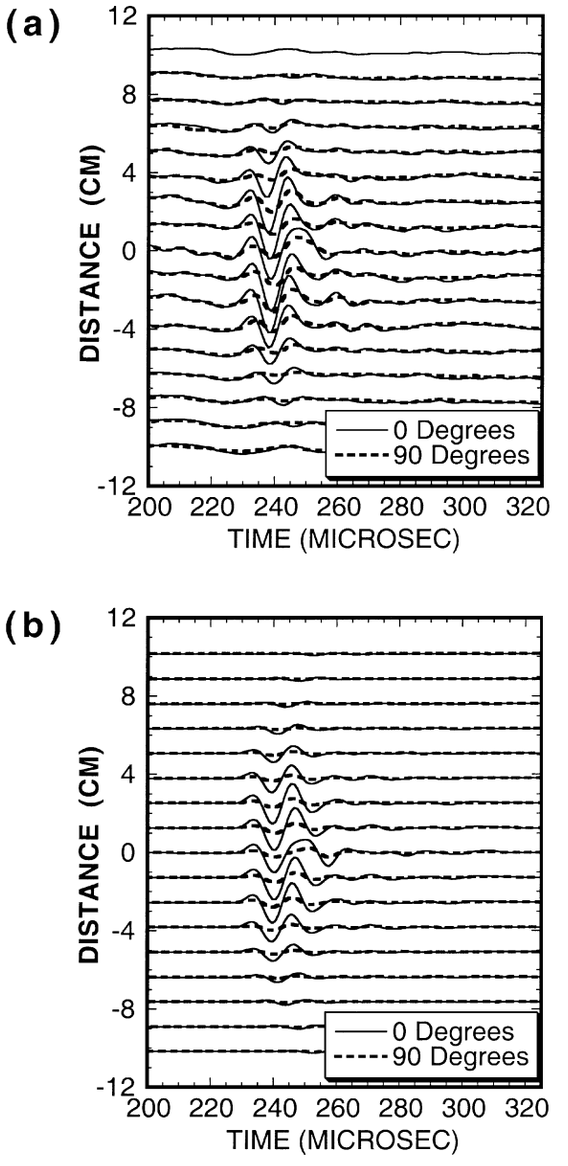

FIG. 4. *SH*-wave data and ray–Born synthetics for the phenolite disk model at the 10° angle of incidence. (a) Data. (b) Synthetics.

main peak in the signal is longer, a pattern that is reproduced accurately in the synthetic seismograms. These waveform variations we see at the center of the disk are caused by the energy scattered from the edge of the disk. When the source and receiver, are precisely centered over the disk, the configuration is symmetric about the vertical plane defined by the source, receiver, and specular reflection points. Energy scattered from the edge of the disk arrives simultaneously from the two sides of the symmetry plane and adds constructively, creating a signal that arrives after the first arrival reflected from the center of the disk.

Data collected at incidence angle 45° are fairly similar to the previous results, with a slightly larger contrast in amplitude between the two azimuths (Figure 5). The waveform variations noted in the 10° incidence angle data are evident in these physical and numerical modeling results as well.

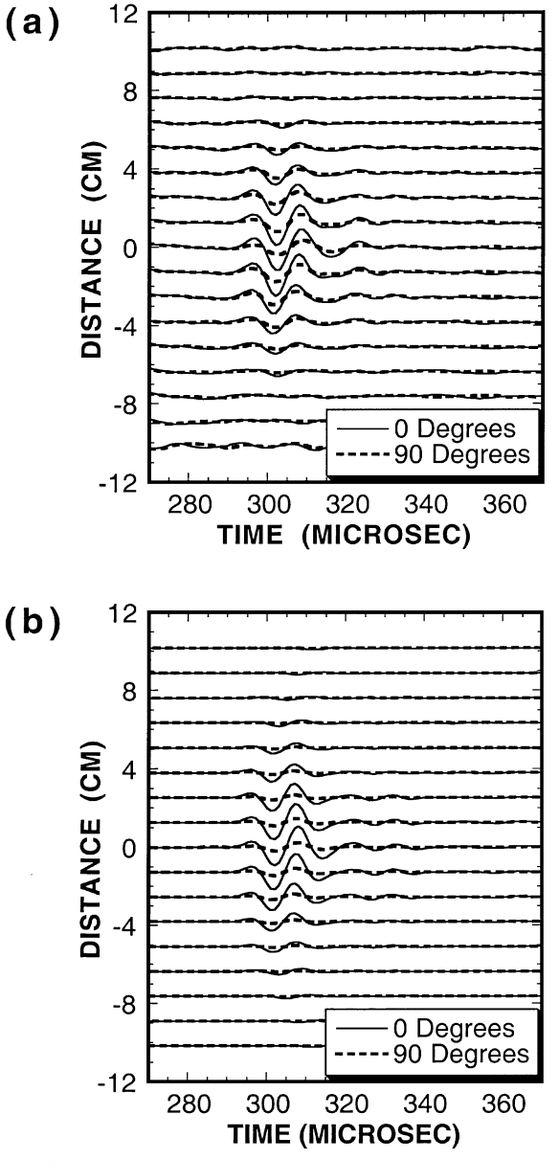

FIG. 5. *SH*-wave ultrasonic data and ray-Born synthetic seismograms for angle of incidence 45°. (a) Data. (b) Synthetics.

Figure 6 compares the rms reflection amplitude profiles across the disk for the data and synthetics, results that allow a more quantitative assessment of the model's accuracy. These amplitude measurements were normalized by the amplitude of the center trace at azimuth 0° to compensate for any differences in source magnitude between synthetic results and data. The shapes of the amplitude curves for the synthetic seismograms are very similar to the data. The primary difference between the synthetics and the data is that the contrast in amplitude as source–receiver azimuth changes from 0 to 90° is overpredicted. For example, at the distance coordinate 0 cm, the center of the disk, the synthetics display a contrast of 3.70 while the data result is 2.13. Similar comments hold for the rms amplitudes measured from the 45° angle of incidence data, though the errors are somewhat smaller and the measurements show less apparent scatter (Figure 6b). The error in the ray–Born method is not surprising since the contrasts in material properties are rather strong. The difference in velocity between lucite and phenolite at the 90° azimuth is about 1%—a reasonable value for the Born approximation—but the same value for the 0° azimuth is about 38%.

Ray tracing—modeling of tuning effects

The *P*-wave data acquired from the physical model show lateral amplitude variations that are very similar to those observed and modeled in the *SH*-wave data (Figure 7). As noted above, the ray–Born algorithm produces much less satisfactory

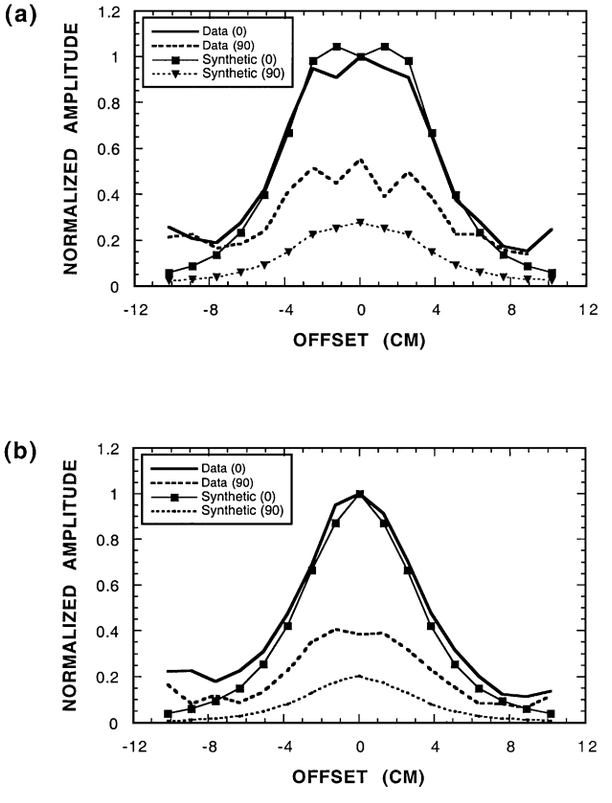

FIG. 6. The rms amplitudes of reflected wavefields in *SH*-wave synthetic data and ray–Born synthetic seismograms: (a) 10° angle of incidence, (b) 45° angle of incidence.

results for the *P*-wave data, so we do not present them here. This failure is probably because the source spectrum contains a much broader frequency range than does the *SH*-wave source (Figure 3). In particular, the spectrum of the *SH*-wave source decreases in magnitude very quickly away from the center frequency (85 kHz), while the *P*-wave source has significant energy out to frequencies about 2.5 times the center frequency (200 kHz). Since the Born approximation works best for low frequencies (i.e., long wavelengths relative to the size of velocity perturbations), it will be more difficult to apply in this case.

Ray tracing can still provide a model of amplitude dependence on angle of incidence and azimuth, though it cannot reproduce the amplitude and pulse shape variations associated with scattering from the disk edge. Figure 8 displays the synthetic seismograms for both the *SH*- and *P*-waves, where we utilized the measured source wavelets for both wave types in the modeling. The 1-D ray-tracing model has identical dimensions to the physical model used for ultrasonic data acquisition (Figure 1), except that we assume a simple phenolite layer instead of a disk. Synthetic traces are shown for a range of angles of incidence that include the values used in the experiment. The *P*-wave synthetics show little difference in amplitude between azimuths, while the *SH*-wave results show similar ratios to those measured in the data.

Since there is a large difference in quasi-compressional wave velocities between azimuths at large angles of incidence in the phenolite (Figure 2), the lack of amplitude variation with azimuth must be a consequence of the tuning of reflections from the top and bottom of the layer. Such tuning phenomena are a well-known cause of waveform variations in isotropic media (Sheriff and Geldart, 1995). When tuning is an important factor controlling amplitude and phase of data, the frequency content of the source signal is also important. Figure 9 shows *P*-wave synthetic seismograms for an angle of incidence of 45° and source frequencies ranging from 200 kHz to 1 mHz, clearly showing how the reflections from the top and bottom of the phenolite superpose at lower frequencies. In particular, at 200 kHz, the dominant frequency of our *P*-wave data, no difference is visible between data acquired with azimuths of 0°

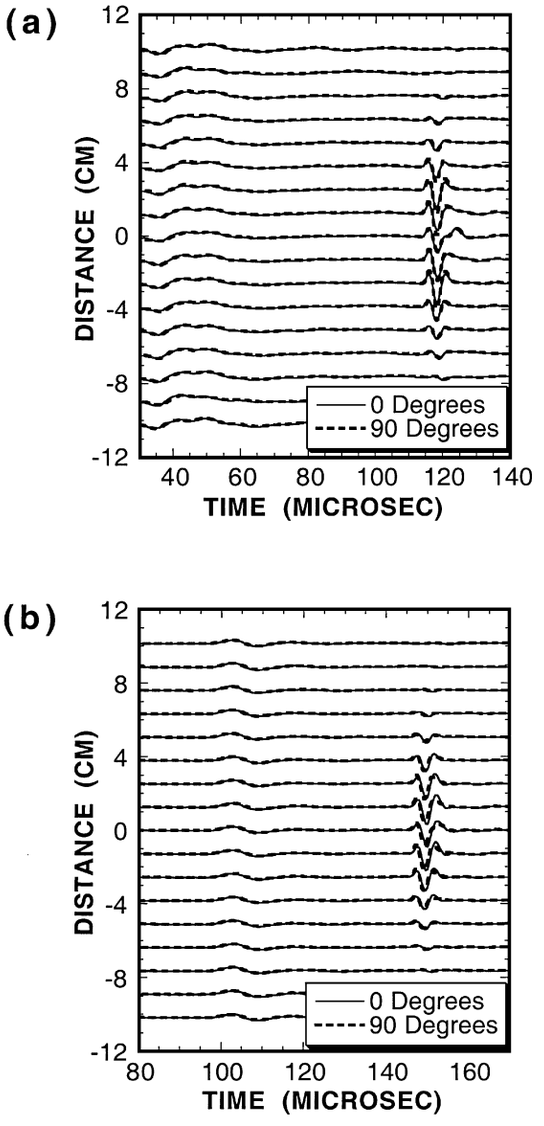

FIG. 7. *P*-wave ultrasonic data: (a) 10° angle of incidence, (b) 45° angle of incidence.

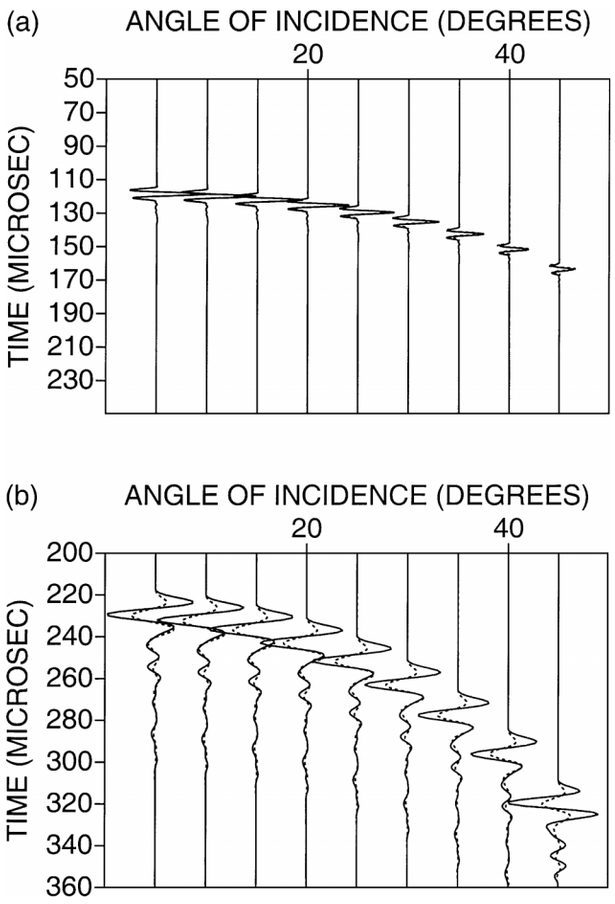

FIG. 8. (a) *P*-wave and (b) *SH*-wave synthetic seismograms from ray tracing for a range of angles of incidence. The solid lines indicate synthetic seismograms for the 0° acquisition azimuth, while dashed lines indicate the 90° azimuth.

and 90°. Large differences are visible for higher frequencies, however, and the variable tuning effects actually cause an exaggerated azimuthal contrast in amplitude at frequencies around 400 kHz.

FIELD-SCALE MODELS OF TUNING EFFECTS

These ultrasonic data and numerical modeling results demonstrate how tuning can have a significant impact on azimuthal AVO analyses. Further ray-tracing studies also show that such tuning effects can either diminish or enhance azimuthal AVO response in fractured reservoir models of realistic dimensions and for realistic frequency ranges.

As a simple model of an anisotropic fractured material, we consider an isotropic rock with velocities $V_p = 6.1$ km/s, $V_s = 3.27$ km/s, and density $= 2.7$ g/cm^3. We then apply the second-order Hudson theory (Hudson, 1980, 1981) to approximate elastic constants of the transversely isotropic material, which has a horizontal axis of symmetry that is perpendicular to the x-axis in our coordinate system. The computed constants are shown in Table 2. The model used to compute synthetic seismograms contains an isotropic layer of constant thickness, 1 km, overlying the fractured layer, which overlies an isotropic half-space of the same velocity as the uppermost layer. These isotropic velocities are $V_p = 4.5$ km/s and $V_s = 3.0$ km/s. Note that the vertical P-wave velocity in the anisotropic layer is 5.89 m/s, about 30% faster than the isotropic layer. On the other hand, the minimum phase velocity, in the direction perpendicular to the fractures, is 4.70 m/s—only 4.4% faster than the isotropic layer.

The source frequency was fixed at 30 Hz for all calculations, and we changed the layer thickness to test various ratios of wavelength to layer thickness. Examples of synthetic seismograms show a tuned response that appears to contain only a single reflection (Figure 10a) for a relatively thin 0.05-km layer and the completely detuned response for a 0.3-km reservoir (Figure 10b).

The reflection responses for a broad range of reservoir thicknesses are shown in Figure 11, where the AVO gradient and

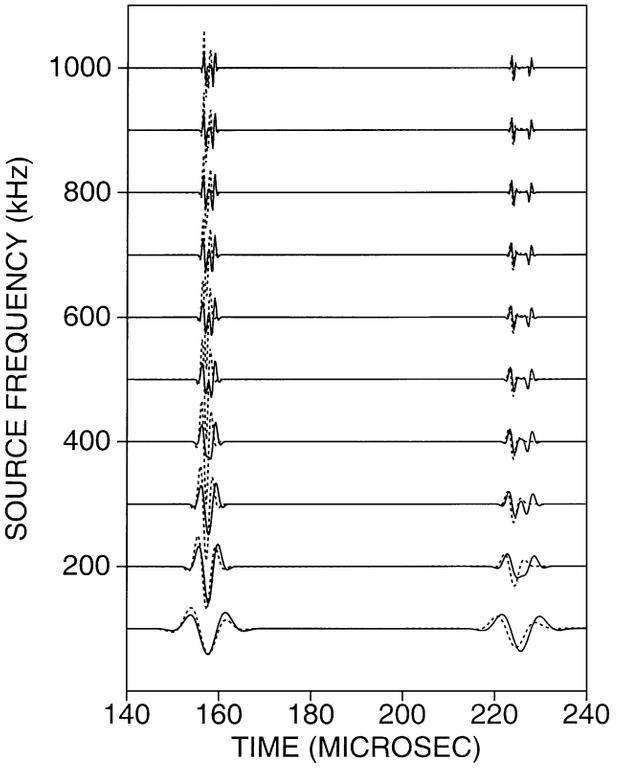

FIG. 9. P-wave ray-tracing synthetic seismograms for a model similar to the physical model displayed in Figure 1 but with a simple phenolite layer rather than a disk. The solid lines indicate synthetic seismograms for the 0° acquisition azimuth, while dashed lines indicate the 90° azimuth. The synthetic seismograms, computed for a 45° angle of incidence, were convolved with source wavelets with central frequencies ranging from 100 kHz to 1 MHz. The seismograms were computed for a downgoing P-wave and included both P- and S-waves reflected from the top and bottom of the phenolite layer.

Table 2. Elastic constants for the anisotropic fractured layer utilized in ray-tracing calculations. The density of the layer is 2.7 g/cm^3.

58.35	25.25	25.25	0.	0.	0.
25.25	91.61	35.29	0.	0.	0.
2.25	35.29	91.61	0.	0.	0.
0.	0.	0.	28.16	0.	0.
0.	0.	0.	0.	22.63	0.
0.	0.	0.	0.	0.	22.63

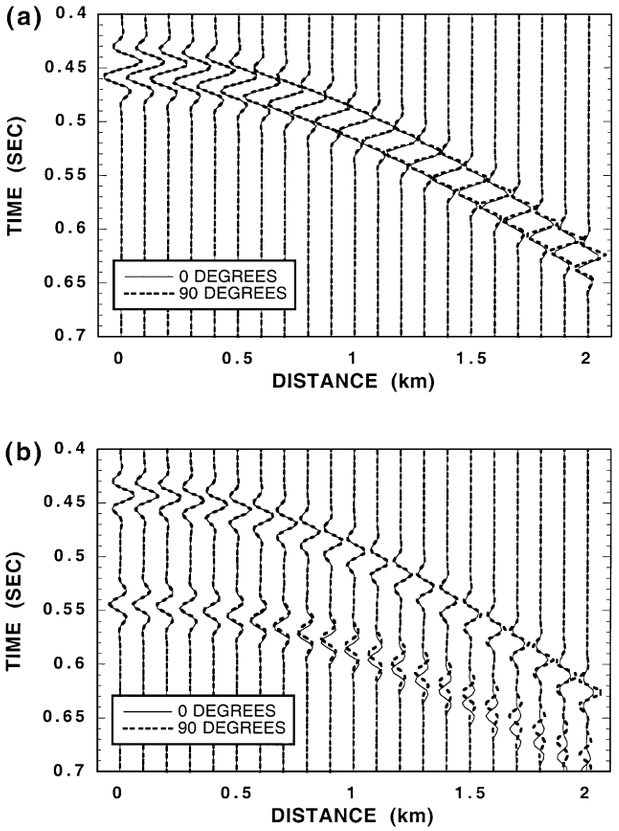

FIG. 10. P-wave synthetic seismograms for the geological model described in the text. The anisotropic fractured layer is (a) 0.05 and (b) 0.3 km thick.

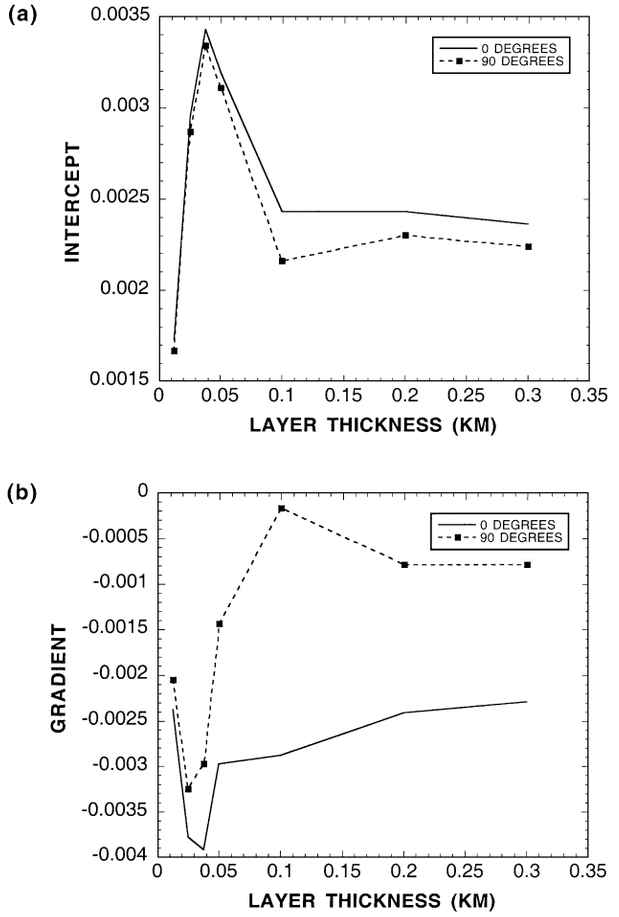

FIG. 11. AVO parameters for the single-layer reservoir model described in the text. Example synthetic seismograms are shown in Figure 10. (a) Intercept. (b) Gradient.

intercept are plotted. These parameters are computed using conventional AVO analyses, where we fit the reflected amplitude to a simple equation that is linear in $\sin^2\theta$, where θ is angle of incidence (Shuey, 1985):

$$R_p(\theta) = A + B\sin^2\theta. \tag{5}$$

The variations in tuning cause dramatic variations in AVO response as the target layer thickness varies. In addition, because of the azimuthal changes in reservoir velocity, the contrast between the response parallel (0°) and perpendicular (90°) to the fracture trend changes.

For this particular model, the thinnest layers, those less than about 25 m, create a situation where the azimuthal AVO response is masked by the tuning of reflections from the upper and lower interface. For the large thicknesses > 100 m, the reflection is completely detuned (see Figure 10b) and the AVO intercept and gradient reach a constant value. The response is most interesting for the intermediate thicknesses, where the tuning is highly variable and the contrast in measured properties between the azimuths of 0° and 90° is very large. This type of behavior may occur in natural settings and could help to explain cases where an azimuthal AVO contrast can be measured even where the quasi-*P*-wave reflection coefficients are not expected to generate a measurable azimuthal AVO signature.

CONCLUSIONS

An ultrasonic experiment was designed to model azimuthal AVO signatures such as those associated with fractured reservoirs in field settings. The ultrasonic data acquired for an *SH*-wave source and a receiver displayed clear azimuthal variations, and the variations in waveforms could be modeled accurately using a ray–Born technique. There were some errors in absolute amplitudes computed with the ray–Born method because of the large contrasts in properties between phenolite and lucite.

In contrast, our *P*-wave data acquired along azimuths oriented at 0° and 90° to the *x*-axis did not display large variations in azimuthal AVO response, even though the quasi-compressional-wave phase velocity changed fairly rapidly with azimuth. This lack of azimuthal AVO response was a consequence of the tuning of reflections from the top and bottom of the phenolite disk layer representing the reservoir layer in the physical model. Because the thickness of this reservoir layer was chosen to accurately reproduce scales that could be encountered in field situations, this phenomenon could be important in reservoir characterization work. Additional calculations of synthetic seismograms for a simple one-layer reservoir model showed that traditional AVO parameters, intercept and gradient, are sensitive to the anisotropic, azimuthal variations in tuning. For wavelengths that were large compared to the layer thickness, the azimuthal variation in AVO response was negligible, but the contrast in AVO measurements was actually enhanced for wavelengths comparable to the thickness of the layer. These results demonstrate that analysis of *P*-wave field data for azimuthal variations in AVO can be very challenging, even if data with large angles of incidence are available.

Finally, we note that after this article was completed, a theoretical analysis of azimuthal variations in tuning by Schoenberg et al. (1999) was published. Their conclusions support the implications of our physical and numerical modeling.

ACKNOWLEDGMENTS

The manuscript was improved by the comments of two anonymous reviewers, R. L. Smith, V. Grechka, and G. Schuster. This work was supported by the Department of Energy under the Small Business Innovation Research program, contract DEFG0295ER82066.

REFERENCES

Al-Dajani, A., and Tsvankin, I., 1998, Nonhyperbolic reflection moveout for horizontal transverse isotropy: Geophysics, **63**, 1738–1753.
Ben-Menahem, A., and Beydoun, W. B., 1985, Range of validity of seismic ray and beam methods in general inhomogeneous media—I. General theory: Geophys. J. Roy. Astr. Soc., **82**, 207–234.
Beydoun, W., and Mendes, M., 1989, Elastic ray–Born l2-migration/inversion: Geophys. J., **97**, 151–160.
Beydoun, W. B., and Tarantola, A., 1988, First Born and Rytov approximations: Modeling and inversion conditions in a canonical example: J. Acoust. Soc. Am., **83**, 1045–1055.
Burridge, R., and Beylkin, G., 1990, Linearized inverse scattering problems in acoustics and elasticity: Wave Motion, **12**, 15–52.
Červený, V., 1985, The application of ray tracing to the propagation of shear waves in complex media, *in* Doher, G. P., Ed., Seismic shear waves, part A: Theory: Geophysical Press, 1–124.

Crampin, S., 1978, Seismic wave propagation through a cracked solid: Polarization as a possible dilatancy diagnostic: Geophys. J. Roy. Astr. Soc., **53**, 467–496.
———, 1981, A review of wave motion in anisotropic and cracked elastic media: Wave Motion, **3**, 343–391.
Gibson, R. L., Jr., and Ben-Menahem, A., 1991, Elastic wave scattering by anisotropic obstacles: Application to fractured volumes: J. Geophys. Res., **96**, 19 905–19 924.
Gibson, R. L., Jr., Toksöz, M. N., and Batini, F., 1993, Ray–Born modelling of fracture zone reflections in the Larderello geothermal field: Geophys. J. Internat., **114**, 81–90.
Grechka, V., Theophanis, S., and Tsvankin, I., 1999, Joint inversion of *P*- and *PS*-waves in orthorhombic media: Theory and a physical modeling study: Geophysics, **64**, 146–161.
Hudson, J. A., 1980, Overall properties of a cracked solid: Math. Proc. Camb. Phil. Soc., **88**, 371–384.
———, 1981, Wave speeds and attenuation of elastic waves in material containing cracks: Geophys. J. Roy. Astr. Soc., **64**, 133–150.
Hudson, J. A., and Heritage, J. R., 1981, The use of the Born approximation in seismic scattering problems: Geophys. J. Roy. Astr. Soc., **66**, 221–240.
Johnson, W. E., 1995, Direction detection of gas in pre-Tertiary sediments?: The Leading Edge, **14**, 119–122.
Leary, P. C., and Henyey, T. L., 1985, Anisotropy and fracture zones about a geothermal well from *P*-wave velocity profiles: Geophysics, **50**, 25–36.
Lefeuvre, F., Turpening, R., Caravana, C., Born, A., and Nicoletis, L., 1993, Vertical open fractures and shear-wave velocities derived from VSPs, full waveform acoustic logs, and televiewer data: Geophysics, **58**, 818–834.
Lewis, C., Davis, T. L., and Vuillermoz, C., 1991, Three-dimensional multicomponent imaging of reservoir heterogeneity, Silo field, Wyoming: Geophysics, **56**, 2048–2056.
Lynn, H. B., Bates, C. R., Simon, K. M., and Van Dok, R., 1995, The effects of azimuthal anisotropy in *P*-wave 3-D seismic: 65th Ann. Internat. Mtg., Soc. Expl. Geophys., Expanded Abstracts, 727–731.
MacBeth, C., Zeng, X., Yardley, G., and Crampin, S., 1994, Interpreting data matrix asymmetry in near-offset, shear-wave VSP data: Geophysics, **59**, 176–191.
Mallick, S., and Fraser, L. N., 1991, Reflection/transmission coefficients and azimuthal anisotropy in marine studies: Geophys., J. Internat., **105**, 241–252.
Martin, M. A., and Davis, T. L., 1987, Shear-wave birefringence: A new tool for evaluating fractured reservoirs: The Leading Edge, **6**, 22–28.
Meadows, M. A., and Winterstein, D. F., 1994, Seismic detection of a hydraulic fracture from hear-wave VSP data at Lost Hills field, California: Geophysics, **59**, 11–26.
Pérez, M., Gibson, Jr., R. L., and Toksöz, M. N., 1999, Detection of fracture orientation using azimuthal variation of *P*-wave AVO reponses: Geophysics, **64**, 1253–1265.
Rüger, A., 1998, Variation of *P*-wave reflectivity with offset and azimuth in anisotropic media: Geophysics, **63**, 935–947.
Rüger, A., and Tsvankin, I., 1997, Using AVO for fracture detection: Analytic basis and practical solutions: The Leading Edge, **16**, 1429–1438.
Schoenberg, M., and Helbig, K., 1997, Orthorhombic media: Modeling elastic wave behavior in a vertically fractured earth: Geophysics, **62**, 1954–1974.
Schoenberg, M., Dean, S., and Sayers, C., 1999, Azimuth-dependent tuning of seismic waves reflected from fractured reservoirs: Geophysics, **64**, 1160–1171.
Sheriff, R. E., and Geldart, L. P., 1995, Exploration seismology 2nd ed.: Cambridge Univ. Press.
Shuey, R., 1985, A simplification of the Zoeppritz equations: Geophysics, **50**, 609–614.
Thomsen, L., 1988, Reflection seismology over azimuthally anisotropic media: Geophysics, **53**, 304–313.
Tsvankin, I., 1997, Anisotropic parameters and *P*-wave velocity for orthorhombic media: Geophysics, **62**, 1292–1309.
Winterstein, D. R., 1986, Anisotropy effects in *P*-wave and *SH*-wave stacking velocities contain information on lithology: Geophysics, **51**, 661–672.
Wu, R. S., and Aki, K., 1985, Scattering characteristics of elastic waves by an elastic heterogeneity: Geophysics, **50**, 585–595.